Special issue article

JDMS

Journal of Defense Modeling and Simulation: Applications, Methodology, Technology
1–17

DOI: 10.1177/15485129261436073
journals.sagepub.com/home/dms
Sage

Modeling drone swarms with a PDE extension of Lanchester's laws

Charles Randow[1], Ryan H Allaire[1], Antonio Mastroberardino[1], and Ruixi Luo[1]

Abstract

We extend the Lanchester equations of combat modeling by constructing a coupled system of partial differential equations with the goal of representing engagements between an attacking drone swarm and a layered defense. Our model includes an attacking force of drones traversing the battlefield (domain) in an attempt to reach its target. The defending force, which engages the incoming attackers, is made up of a static defense and a mobile drone force capable of intercepting and tracking the attackers. Drone swarm motion is modeled with advection–diffusion terms and engagement at range by nonlocal reaction terms. We solve the underlying model using a finite difference method and investigate how interaction range, swarm dispersion, and the allocation between static and mobile defenses affect attacker survivability. To account for expendable or single-use countermeasure platforms (e.g. kamikaze–style interceptors), we also examine how expendability affects the final engagement outcome. This study provides a foundation for modeling spatially distributed combat dynamics reflecting current and future combat scenarios.

Keywords

Partial differential equations, Lanchester equations, combat modeling

1. Introduction

Combat modeling is a multidisciplinary endeavor that uses mathematical, computational, and simulation techniques to analyze, predict, and optimize military operations. Over the past century, research has evolved from simple tabletop wargames to sophisticated mathematical models involving ordinary differential equations (ODEs) or partial differential equations (PDEs) to account for various aspects of combat such as intelligence, maneuvering, terrain, and spatial-temporal dynamics.

Introduced during World War I, Lanchester equations[1] model the losses, called attrition, of opposing forces using a system of ODEs and form the basis for much of modern combat modeling. The original Lanchester system of ODEs assumes constant effectiveness of weapons over time in either one of two scenarios.

The first scenario is based on a model that assumes constant aimed fire in which each force suffers attrition proportional to the size of the opposing force:

$$\frac{dM_1}{dt} = -aM_2 \tag{1}$$

$$\frac{dM_2}{dt} = -bM_1 \tag{2}$$

where M_1 and M_2 represent the sizes of two forces and a and b model the effectiveness of each force. We use the symbols M_1 and M_2 since we will be referring to the size of a force as its mass, which is helpful when PDEs are introduced in section 2. Equations (1) and (2) can be solved directly by dividing the second equation by the first and then using separation of variables to obtain the well-known square law.

The second scenario is based on a model that assumes constant area fire in which attrition is proportional to the product of the masses of both forces:

[1]United States Military Academy, USA

Corresponding author:
Charles Randow, Department of Mathematical Sciences, United States Military Academy, 646 Swift Road, West Point, NY 10996, USA.
Email: charles.randow@westpoint.edu

$$\frac{dM_1}{dt} = -aM_1M_2 \tag{3}$$

$$\frac{dM_2}{dt} = -bM_1M_2 \tag{4}$$

The area fire model can be solved by dividing Equation (3) by Equation (4) to obtain the linear law, where trajectories are lines with slope a/b. For both the aimed fire (square law) and area fire (linear law) scenarios, the initial conditions $M_1(0)$ and $M_2(0)$ and the attrition ratio a/b determine the final outcome of the conflict being modeled.

Despite their frequent use and mathematical simplicity, these equations are predicated on a number of fundamental assumptions that may limit their applicability to contemporary warfare. A limitation of the classical Lanchester models is their lack of a spatial dimension, with the classical models assuming continuous, homogeneous engagement where an entire force can, in theory, engage the opposing force at all times. This classical model assumption, described as a homogeneous mixing of forces, fails to account for critical tactical realities such as ranged firepower, maneuver, and varying troop effectiveness,[2] underscoring the need for more sophisticated mathematical frameworks.

Perhaps the first attempt to address the assumption of homogeneity present in the classical models came from Deitchman who modeled asymmetric conflict.[3] This model combined the aimed fire model and the area fire model into a single system demonstrating that different forces could operate under different attrition laws simultaneously, providing a more realistic representation of conflicts involving irregular warfare.

Another researcher who addressed the shortcomings of the classical Lanchester system was Bonder whose research focused on the formalization of the attrition rates. The goal of his work was to precisely define and measure the variables that influence attrition on the battlefield.[4] This effort to quantify aspects of combat was a necessary precursor to later work on time-dependent coefficients. Bonder's contributions represented a crucial shift from abstract theory to an applied, data-driven approach, preparing the groundwork for a new generation of models that would be more responsive to the dynamic nature of military operations.

In the 1970s, Taylor and his research collaborators recognized that in actual combat, effectiveness of enemy fire changes because of factors like weather, terrain, fatigue, logistics, reinforcements, and morale.[5–10] To account for these factors, the Lanchester system of ODEs was extended to include time-dependent attrition rates. In some special cases, they derived closed-form analytical solutions or used integral transforms and approximations when general solutions were not possible. The various formulations allowed modeling of periodic changes such as seasonality, weather patterns, or step changes such as arrival of reinforcements or depletion of ammunition, but still did not account for spatial considerations.

Beginning in the late 1980s, Protopopescu et al.[11–14] proposed models based on coupled nonlinear PDEs to describe the evolution of opposing forces in combat. Their models capture spatial dynamics such as maneuver and terrain affects, in both one and two spatial dimensions, by incorporating diffusion terms for random spreading of troops, advection terms for ordered movement, and interaction terms for attrition. More recently, Keane[15] proposed an alternative framework using PDEs that include nonlocal terms, a concept adopted from biological aggregation models for swarming behavior,[16] to simulate spatially coherent troop dynamics.

The Lanchester equations and their variations continue to provide a foundational framework for reasoning about force concentration and attrition in combat. Building on this tradition, we develop a spatially explicit modeling framework motivated by a contemporary defense scenario:[17] a drone swarm attempting to penetrate a layered defense. We construct a coupled system of PDEs that incorporates advection–diffusion for movement and nonlocal reaction terms to simulate ranged engagement. Our model separates the defending force into a static defense and a mobile drone (dynamic) defense capable of tracking the attacking drone swarm. Within this abstract and idealized setting, we investigate how interaction range, swarm dispersion, and the allocation of defensive resources affect the attacker's survivability. Furthermore, we examine the efficiency of expendable countermeasure platforms. The results are intended to illustrate qualitative behaviors and trade-offs inherent in the model formulation, rather than to provide operational predictions or technology-specific performance assessments.

2. Model formulation

Let $f_1(x,t), f_2(x,t)$, and $f_3(x)$ be the density fields of the attacking drone swarm, the defending drone swarm with tracking capabilities (called the dynamic defense), and the static defense, respectively. The attacking drones and the dynamic defense are assumed to move with velocities u_1 and u_2 on a one-dimensional domain $\Omega = [0, L]$. We model the evolution of the attacking force and the dynamic defense with a (dimensionless) modified system of advection–diffusion equations:

$$\frac{\partial f_1}{\partial t} + \frac{\partial}{\partial x}(u_1 f_1) = \mathcal{D}_1 \frac{\partial^2 f_1}{\partial x^2} - \mathcal{R}_1(f_1, f_2, f_3) \tag{5}$$

$$\frac{\partial f_2}{\partial t} + \frac{\partial}{\partial x}(u_2 f_2) = \mathcal{D}_2 \frac{\partial^2 f_2}{\partial x^2} - \mathcal{R}_2(f_1, f_2) \tag{6}$$

The second term in each equation represents the movement (advection) of the attacking and defending drone swarms, where u_1 and u_2 are the corresponding velocities. The third term represents diffusion, with dimensionless diffusivities $\mathcal{D}_1$ and $\mathcal{D}_2$ (effectively inverse Peclét numbers) that model the natural tendency of swarms to spread out from their initial configurations through small-scale movement.

The rightmost terms in Equations (5) and (6) are reaction terms that represent interactions between the opposing forces. The term $\mathcal{R}_1$ controls the effectiveness of the defender's fire (both dynamic and static) against the attacking drone force. The term $\mathcal{R}_2$ allows for attrition due to single-use or expendable defending drones; it is not intended to model any fire from the attacking force directed against the dynamic defense. The negative sign preceding each reaction term reflects that combat interactions contribute to attrition, decreasing the densities f_1 and f_2.

Equations (5) and (6) are written in nondimensional form using characteristic spatial and temporal scales. Consequently, the spatial coordinate x, domain length L, time t, and the velocities u_1 and u_2 are dimensionless quantities. In addition, the density fields (f_1, f_2, and f_3) are scaled by a characteristic force level so that they represent relative dimensionless force densities. Under this scaling, the diffusivities and reaction coefficients are likewise dimensionless parameters.

As discussed in section 1, the masses of each force will be used in our analysis, where mass is computed by integrating the density as follows:

$$M_i = \int_\Omega f_i(x, t)\, dx, \text{ for } i = 1, 2$$

Since both x and f_i are nondimensional, the masses M_i are likewise dimensionless quantities. Throughout this work, the initial masses are $M_i(0) = 1$, so that $M_i(t) < 1$ represent the fraction of the remaining force. For example, $M_1 = 0.75$ means that 75% of the attacking force remains. We also assume that the attacking drone swarm does not fire on the static defense so that its density f_3 remains constant in time and thus $M_3 = 1$ is constant throughout our simulations.

In this study, we follow the work of Protopopescu et al.[13] to formulate the reaction terms in Equations (5) and (6). We define $\mathcal{R}_1$ to be the sum of two nonlocal reactions, one associated with a dynamic defense $\mathcal{R}_{1_D}$ and one with a static defense $\mathcal{R}_{1_S}$, such that

$$\mathcal{R}_1 = \mathcal{R}_{1_D} + \mathcal{R}_{1_S}$$

where

$$\mathcal{R}_{1_D} = k_2 f_1(x, t) \int_\Omega K_D(x - y) f_2(y, t)\, dy$$

$$\mathcal{R}_{1_S} = k_3 f_1(x, t) \int_\Omega K_S(x - y) f_3(y)\, dy$$

The effectiveness (or combat strength) of the dynamic defense is given by k_2, and the effectiveness of the static defense is given by k_3 (these parameters are known as Damköhler numbers). The distance-dependent kernel is given by K_D for the dynamic defense and by K_S for the static defense. Although many forms exist for such a kernel (e.g. Gaussian,[18] exponential[15]), we will use the compactly supported cosine interaction kernel:

$$K_i(r) = \begin{cases} \frac{1}{2}\left(1 + \cos\left(\frac{\pi r}{\rho_i}\right)\right), & |r| \le \rho_i \\ 0, & \text{otherwise,} \end{cases}$$

where $i = D$ for the dynamic defense kernel and $i = S$ for the static defense kernel. The interaction ranges ρ_D and ρ_S for the defenders are positive parameters.

We account for expendable or single-use defending drone swarms using the reaction term $\mathcal{R}_2$, where

$$\mathcal{R}_2 = \alpha k_2 f_2(x, t) \int_\Omega K_D(x - y) f_1(y, t)\, dy$$

Comparing $\mathcal{R}_{1_D}$ and $\mathcal{R}_2$, we observe that the two terms share the same nonlocal interaction structure, differing only through the factor α. The term $\mathcal{R}_2$ allows the dynamic defense to incur losses proportional to the attacking force. For example, $\mathcal{R}_2$ could be used to model a kamikaze-type countermeasure, where defending drones are destroyed in the process of engaging attackers. It could also be used to model a single-use countermeasure that, once deployed, leaves the defending drone incapable of engaging additional attackers. In sections 3.4 and 3.5, we will examine this type of dynamic defense.

Consider the following values for the expendability parameter α: $\alpha = 0$, $0 < \alpha < 1$, $\alpha = 1$, and $\alpha > 1$. If $\alpha = 0$, the dynamic defense is nonexpendable (as is the static defense in the present work), suffering no attrition while causing losses to the attackers. The case of $\alpha = 1$ indicates a one-for-one offense-defense, such that attrition inflicted on the attacking force by the dynamic defense is also inflicted on the dynamic defense. Interactions with $0 < \alpha < 1$ correspond to a relatively greater efficiency for the defense, compared with the $\alpha = 1$ case. In this situation, the defender suffers less relative attrition while engaging the attacker. Conversely, when $\alpha > 1$, the dynamic defense is less efficient and so the defender suffers greater

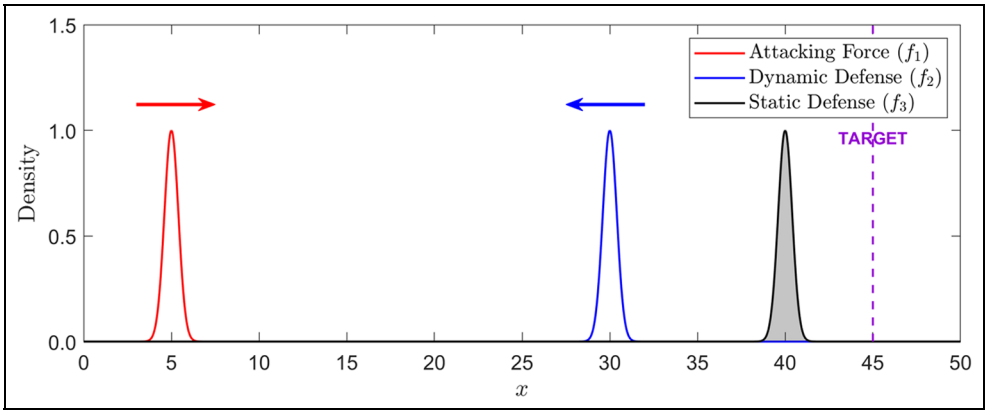

Figure 1. Schematic of an initial condition used for simulations, showing the attacking force (left), dynamic defense (center), and static defense (right). The dashed line indicates the final target for the attacking force.

attrition. For example, in the case of kamikaze defending drones, $\alpha < 1$ if a single defender destroys more than one attacker, while for $\alpha > 1$, multiple defending drones are required to eliminate a single attacker.

The three densities representing the attacking drone swarm, the dynamic defense, and the static defense are initialized with Gaussian profiles:

$$f_i(x, t=0) = \frac{1}{\sigma_i\sqrt{2\pi}} e^{-(x-x_i)^2/2\sigma_i^2}, \qquad i = 1, 2, 3$$

centered at x_1, x_2, and x_3, with spreads (widths) characterized by σ_1, σ_2, and σ_3. The static defense maintains its distribution for all time.

It should be noted that the choice of σ_i controls the degree to which each force is initially concentrated or spread out in space. For simplicity, we choose the characteristic spread $\sigma_1 = \sigma = 1/\sqrt{2\pi}$; we use σ as a reference length scale, characterizing the initial spatial footprint of the attackers. Unless otherwise stated, for the defense, we use $\sigma_2 = \sigma_3 = \sigma$, so that both the initial height of f_i and its mass, M_i, are set to 1.

Figure 1 shows a sample initial condition. The red distribution represents the attacking drones which move from their initial position to the left to reach the target (violet dashed curve). The defense comprised a dynamic defense (blue) and a static defense (black/shaded gray). Notably, the dynamic defense initially travels leftward, then interacts with the attackers once within range, and finally follows (tracks) the attackers to continually engage with the attackers. To implement this tracking, we first define the intermediate velocity

$$U(t) = \gamma\left(\overline{M}_1(t) - \overline{M}_2(t)\right)$$

where $\overline{M}_i(t) = M_i^{-1}\int x f_i(x, t)\, dx$, $i = 1, 2$, are the centers of mass of the attacking drones and the dynamic defense, respectively, and γ is a proportional gain factor, representing the responsiveness of the defense to separation from the attackers. The magnitude of this velocity (speed) is high when the defenders are far from the attackers and low when they are close. To avoid unrealistic speeds and their associated numerical instabilities, we impose the speed limit $|u_2| \le u_{max}$. The actual defender velocity is then given by

$$u_2(t) = \min\left(\max\left(U(t),\ -u_{\max}\right), u_{\max}\right) \tag{7}$$

At the lateral boundaries, $x = 0, L$, we impose zero diffusive flux boundary conditions: $\partial f_1/\partial x = \partial f_2/\partial x = 0$. These conditions model outflow when combined with an advective treatment that permits forces to exit, but not enter, the domain. Additional information on this advective treatment is presented in section B of the Appendix.

In the absence of advection ($u_1 = u_2 = 0$) and diffusion ($\mathcal{D}_1 = \mathcal{D}_2 = 0$) and in the infinite-range limit ($\rho_D, \rho_S \to \infty$), Equations (5) and (6) can be integrated over the domain Ω to obtain

$$\frac{dM_1}{dt} = -k_2 M_1 M_2 - k_3 M_1 M_3 \tag{8}$$

$$\frac{dM_2}{dt} = -\alpha k_2 M_1 M_2 \tag{9}$$

where the masses of the forces $M_1(t)$, $M_2(t)$, and M_3 are computed from the respective densities f_1, f_2, and f_3, respectively. As stated previously, in our formulation the static defense has constant mass, M_3, and thus, Equations (8) and (9) can be considered as a modified Lanchester

system with both aimed and area fire terms. In addition, these two equations can be solved analytically to yield

$$M_1(t) = \begin{cases} \dfrac{M_2}{\alpha} + \dfrac{k_3 M_3}{\alpha k_2} \ln M_2 + \dfrac{\alpha - 1}{\alpha}, & k_2, \alpha \neq 0 \\ \exp\left(-(k_2 M_2 + k_3 M_3)t\right) & \alpha = 0 \end{cases} \quad (10)$$

The derivation of the solution in Equation (10) for the case $k_2 \neq 0$, $\alpha \neq 0$ is given in section A1 of the Appendix. In the results that follow, we use these solutions as a guide for understanding the effects added beyond the traditional Lanchester model.

It is also interesting to note that the classical Lanchester system for aimed fire given in Equations (1) and (2) can be recovered from Equations (5) and (6) by excluding the advection and diffusion terms and defining the reaction terms to be $\mathcal{R}_1 = -af_2$ and $\mathcal{R}_2 = -bf_1$, where a and b are the attrition rates. Integrating both sides of Equations (5) and (6) over the domain Ω yields the desired result. It is important to note that the classical Lanchester equations represent a spatially aggregated model, which is in contrast to the proposed PDE model that includes spatial dependence. Comparisons between the two types of models are readily made by integrating the density functions over the domain to obtain masses.

3. Results

Here, we discuss the main results found by numerically solving Equations (5) and (6) using an implicit–explicit finite difference scheme. In short, the underlying equations are time-integrated using the Crank–Nicolson (CN) method for the diffusion term and Forward Euler method for the remaining advection and reaction terms. Schemes for hyperbolic PDEs typically encounter challenges in trying to balance high-order accuracy, stability, numerical diffusion, and positivity. In order to deal with these numerical challenges, we follow the work of Keane,[15] implementing a flux limiter on the advective term and enforcing positivity constraints. This limiter helps mitigate spurious oscillations near sharp fronts, and enforcing positivity prevents nonphysical solutions. In Sections A2 and A3 of the Appendix, we show that the advection–diffusion–reaction schemes converge. For more information regarding the numerical algorithm, see section B of the Appendix. The standard parameters to be used are presented in Table 1. When different ranges ρ_D and ρ_S are used in this work, those changes will be noted.

Figure 2 shows snapshots of the solution to Equations (5) and (6) for the initial conditions used in Figure 1 ($x_1 = 5$, $x_2 = 30$, $x_3 = 40$, $k_2 = k_3 = 0.5$, $\alpha = 0$), illustrating the spatiotemporal dynamics of the interacting forces. In Figure 2 frame (a), at $t = 5$, the attackers and the dynamic defense are traveling toward each another but are still too far apart to interact. The two drone swarms have closed the distance in frame (b), at $t = 12.5$, but actually start interacting with one another earlier due to ranged firepower, as seen by the decrease in the attacking force. In frame (c), at $t = 20$, the attackers have moved past the dynamic defense, but the defense closely pursues them while continuing to fire. The attackers feel the presence of both defense forces in frame (d), at $t = 35$, when they reach the static defense and ultimately reach their target in frame (e) at $t = 40$. Since the expendability parameter $\alpha = 0$, the dynamic defense does not suffer attrition during the engagement (and neither does the static defense).

Table 1. List of standard parameters used in simulations.

Parameter	Notation	Value
Domain length	L	50
Max simulation time	t_{final}	40
Distribution width	σ	$1/\sqrt{2\pi}$
Dynamic defense range	ρ_D	3σ
Static defense range	ρ_S	3σ
Attacker velocity	u_1	1.0
Max speed	$u_{\max}$	1.0
Proportional gain factor	γ	1.0
Diffusivity	$\mathcal{D}_1, \mathcal{D}_2$	10^{-5}

3.1. Nonexpendable dynamic defense

In sections 3.1–3.3, we consider the case where the expendability parameter $\alpha = 0$, corresponding to a nonexpendable dynamic defense. For example, a nonexpendable drone swarm could have an infinite ammunition supply or an energy source that permits arbitrarily many counter-drone actions. Throughout this section, the initial centers of the attacking force (f_1), dynamic defense (f_2), and static defense (f_3) are fixed at $x_1 = 5$, $x_2 = 30$, and $x_3 = 22.5$, respectively.

Figure 3 shows the time evolution of the attacker's mass, $M_1(t)$, for four simulations with different values of the dynamic and static defense effectiveness parameters, k_2 and k_3. The first result listed in the legend (dot-dash curve) models effectively infinite interaction ranges by setting $\rho_S = \rho_D = 10^3\sigma$, where the entire domain length is approximately equal to $10^2\sigma$. The remaining three plotted results (solid, dashed, and dotted curves) assume finite interaction ranges, with $\rho_S = \rho_D = 3\sigma$. The shaded regions I–IV will be discussed in the context of the finite-range results.

The infinite-range case (dot-dash curve in Figure 3) uses a mixed dynamic-static defense with $k_2 = k_3 = 0.5$. The dynamic and static defenses engage the attacking force immediately, since the interaction ranges are larger than

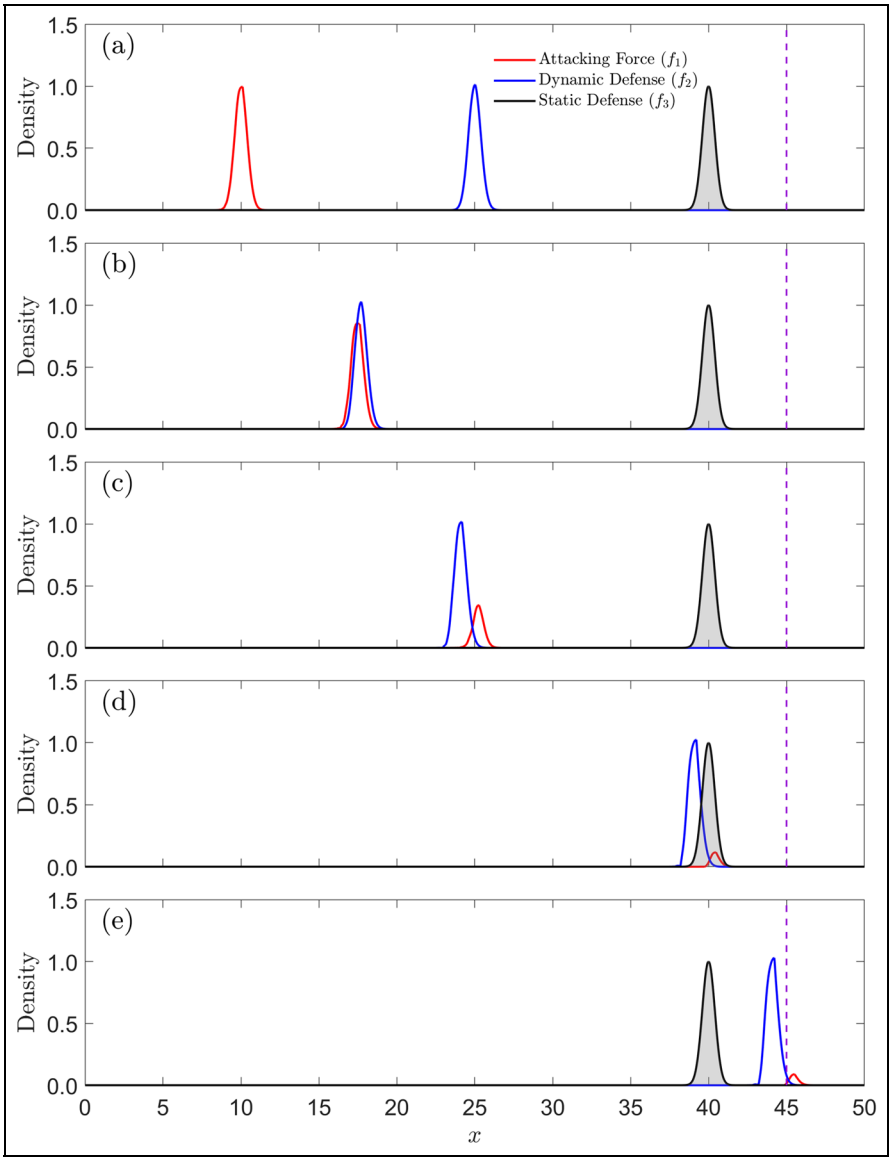

Figure 2. Snapshots of the attacking and defending force densities at (a) $t = 5$, (b) $t = 12.5$, (c) $t = 20$, (d) $t = 35$, and (e) $t = 40$. Here, $k_2 = k_3 = 0.5$ and the initial condition is given in Figure 1, where $x_1 = 5$, $x_2 = 30$, and $x_3 = 40$. Since the expendability parameter $\alpha = 0$, only the attacker suffers attrition.

the domain length. The numerical solution of the PDE decays exponentially in good agreement with the solution for the $\alpha = 0$ case given by Equation (10), which does not have spatial dependence.

The finite-range results in Figure 3 illustrate the effect of different dynamic and static defense effectiveness parameters. The solid curve shows the mass M_1 for a mixed dynamic-static defense, with $k_2 = k_3 = 0.5$. The dashed curve shows the attacker's mass for an exclusively dynamic defense ($k_2 = 0.5$, $k_3 = 0$), while the dotted curve shows results for an exclusively static defense ($k_2 = 0$, $k_3 = 0.5$). There are four regions, noted as I–IV, that highlight the interaction status between the attacking drone force and the two defending forces. Comparing the dynamic-only and static-only cases with the mixed dynamic-static case illustrates the effect of each defense type on the attacking force.

Region I shows a constant mass M_1 since there has been no opportunity for the defenders to interact with the attackers until the attackers and the defenders are in engagement range. In region II, due to the motion of the attackers and dynamic defense, the attacking force will begin to suffer

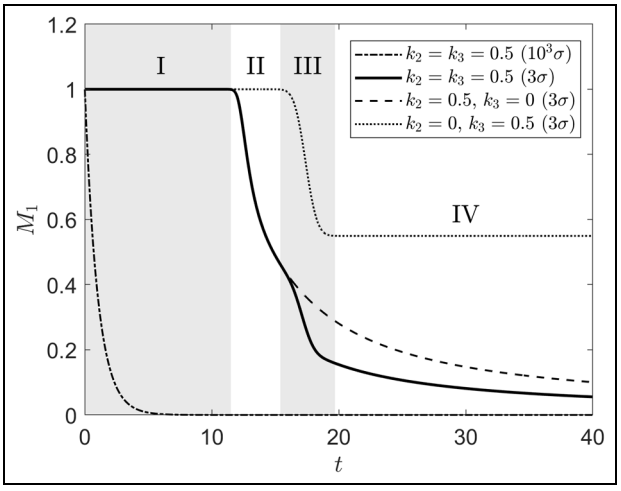

Figure 3. Total mass of the attacking drones, M_1, as a function of time, t, for different values of k_2 and k_3. Ranges are noted in parentheses as either $\rho_S = \rho_D = 10^3\sigma$ or $\rho_S = \rho_D = 3\sigma$. Since $\alpha = 0$, $M_2 = 1$ for all time t.

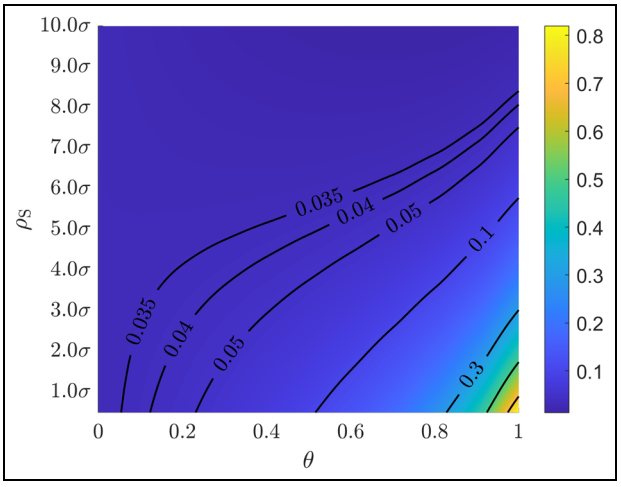

Figure 4. Total mass of the attacking drones $M_1(t)$ after reaching the target (at $t = 40$) for various values of ρ_S and θ, where $\theta = 0$ is dynamic-only and $\theta = 1$ is static-only defense. (Note that $\rho_D = 3.0\sigma$ for all results shown here.) Since $\alpha = 0$, $M_2 = 1$ for all time t.

attrition from the dynamic defense. Initially, there is limited interaction between these two forces due to the finite range, ρ_D. As the attacking force and dynamic defense continue to move toward one another, the attackers completely enter the reach of the dynamic defense, leading to increased attrition of the attackers. Because the dynamic defense tracks the attackers, M_1 continues to decrease even after the forces pass through one another, since the dynamic defense remains within range of the attackers.

In region III, the attacking force also comes into range of the static defense (if a static defense is present), leading to enhanced attrition to M_1. Similarly to the interaction between the dynamic defense and the attackers, the initial interaction with the static defense is limited due to finite range before increasing in effectiveness as the attacking force continues to move through the static defense. However, the attacking force will eventually pass beyond the effective range of the static defense, as shown in region IV. In the static-only defense, this means M_1 remains constant after passing through the static defense.

Figure 3 also illustrates the important role of tracking by considering the different outcomes for the dynamic-only case ($k_2 = 0.5$) and static-only case ($k_3 = 0.5$). Although both combat effectiveness parameters equal 0.5, the dynamic-only defense (with final $M_1 \sim 0.1$) is much more effective than the static-only defense (with final $M_1 \sim 0.55$); this is expected because of the longer interaction time between the attacker and the dynamic defense. Combining both defenses (with $k_2 = k_3 = 0.5$) produces a final mass of $M_1 \sim 0.057$, where all final values are calculated at $t = 40$.

3.2. Distribution of firepower

Here, we discuss the interplay between the dynamic and static defense and their effectiveness on reducing the attacker's mass. For simplicity, we let $K_{eff} = k_2 + k_3 = (1 - \theta)K_{eff} + \theta K_{eff}$ be the effective combat strength of the defense and we set $K_{eff} = 1$. The parameter θ, where $0 \le \theta \le 1$, determines the balance between combat strengths of the dynamic and static defenses. For example, when $\theta = 0$, only the dynamic defense is present with $k_2 = 1$ and $k_3 = 0$. When $\theta = 1$, only the static defense is present with $k_2 = 0$ and $k_3 = 1$. The initial centers for the three forces f_1, f_2, and f_3 are $x_1 = 5$, $x_2 = 30$, and $x_3 = 40$, respectively, as shown in Figure 2.

Figure 4 shows the effect of the static defense range and the balance between dynamic/static firepower on the reduction in the attacker's mass M_1. For a static-only defense ($\theta = 1$) M_1 strongly depends on the range ρ_S since the interaction time is distance dependent; longer range firepower leads to a prolonged engagement with the attackers. Due to the tracking capability, dynamic-defense-oriented forces, associated with small values of θ, cause greater attrition than that of the static-defense-oriented forces. In the case of small θ, supplemental firepower from the static defense minimally reduces M_1, and the range necessary for an equivalent static-only defense requires sufficiently long-range capability. For example, a 95% reduction in the attacking force could be obtained by using 80% dynamic and 20% static defenses ($\theta = 0.2$) at a range of $\rho_S \sim 1.0\sigma$ or a static-only defense ($\theta = 1$) at a range of $\rho_S \sim 7.0\sigma$. It should be emphasized that the apparent

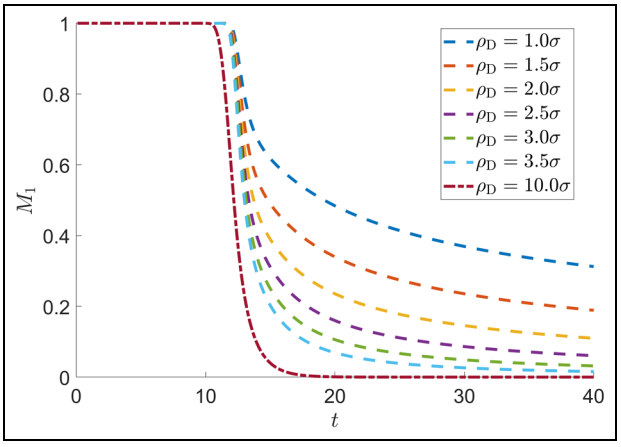

Figure 5. Evolution of the attackers mass M_1 due to the dynamic-only defense ($\theta = 0$) for various values of ρ_D, the dynamic defense range. Since $\alpha = 0$, $M_2 = 1$ for all time t.

advantage of the dynamic defense over the static defense arises from the assumed tracking model permitting longer engagement durations; alternative tracking formulations, which are outside the scope of this paper, may yield different outcomes.

Figure 5 shows the influence that the dynamic defense range has on the attacker's mass M_1 by considering the dynamic-only defense $\theta = 0$. For the $\rho_D = 3.0\sigma$ case of Figure 5, the terminal value of $M_1 = 0.0317$ corresponds to the $\theta = 0$ final mass of Figure 4.

As ρ_D decreases, engagement between the dynamic defense and the attacking forces is delayed, as the initial drop in M_1 shifts to the right in time in Figure 5. Also, as ρ_D decreases, a smaller portion of the defense maintains significant interaction with the attackers during the pursuit. In Figure 2(c), for example, the dynamic defense trails behind the attackers and the shorter the range ρ_D, the less effective the dynamic defense will be as a result.

3.3. Influence of spread

Here, we consider the influence that the initial spread (width) of the distributions has on the model outcomes. The initial centers for the three forces f_1, f_2, and f_3 are $x_1 = 5$, $x_2 = 30$, and $x_3 = 40$, respectively, as in section 3.2. Figure 6 shows the influence that the spread ($\sigma_i = \sigma, 2\sigma, \ldots, 5\sigma$) of the defense has on the final mass of the attacking drones when the defense range (ρ_S or ρ_D) is (a) σ (short-range), (b) 3σ (medium-range), and (c) 10σ (long-range). Note that the horizontal axis range is shortened to $[10, 40]$ in Figure 6 for display purposes. In each of the three cases, the spread of the static defense, σ_3 (solid curves), has little-to-no impact on the final mass M_1. Instead, the final mass M_1 depends only on the static

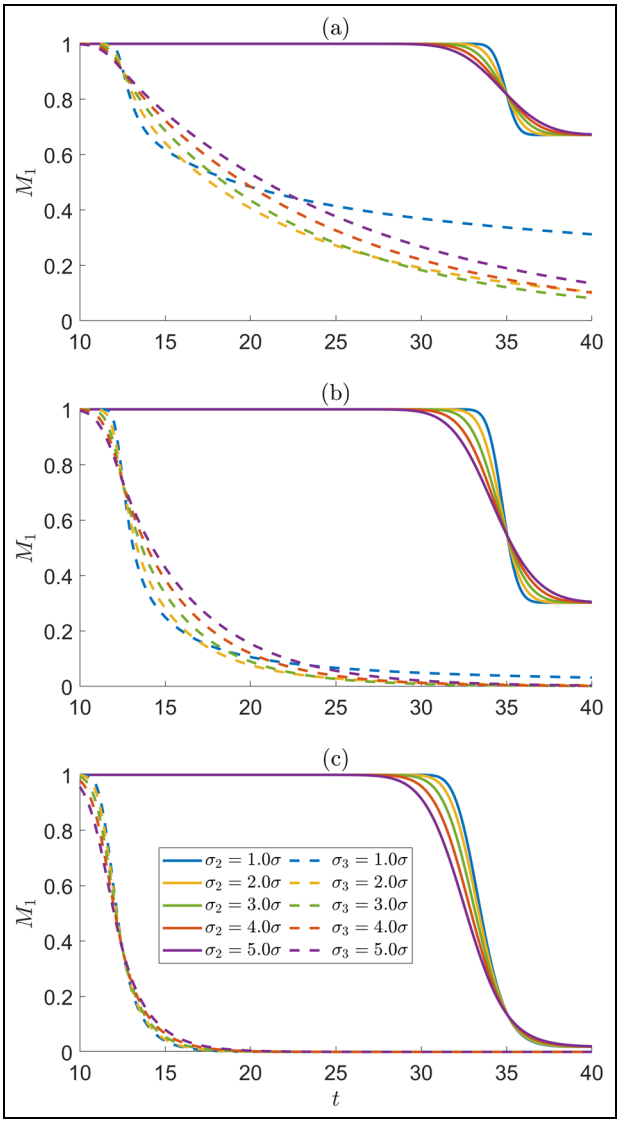

Figure 6. Time evolution of the total mass of f_1 for (a) short-range defense $\rho_S = \rho_D = \sigma$, (b) medium-range defense $\rho_S = \rho_D = 3\sigma$, and (c) long-range defense $\rho_S = \rho_D = 10\sigma$ for $\theta = 0$ (dashed curves) and $\theta = 1$ (solid curves) and for various distribution widths, σ_2 and σ_3. Since $\alpha = 0$, $M_2 = 1$ for all time t.

range ρ_S, mass M_3, and effectiveness k_3. In section A4 of the Appendix, we show that an analytical solution can be found that supports this observation.

The time evolution does depend on σ_3, however, as a more concentrated static defense (solid blue curve) leads to a shorter interaction with an attrition rate higher than defenses with a wider spread. Consequently, the spread matters more when the attackers do not completely pass through the static defense. Consistent with Figure 4, increasing ρ_S increases the attrition of the attackers. This weak dependence on the spread of the static defenders

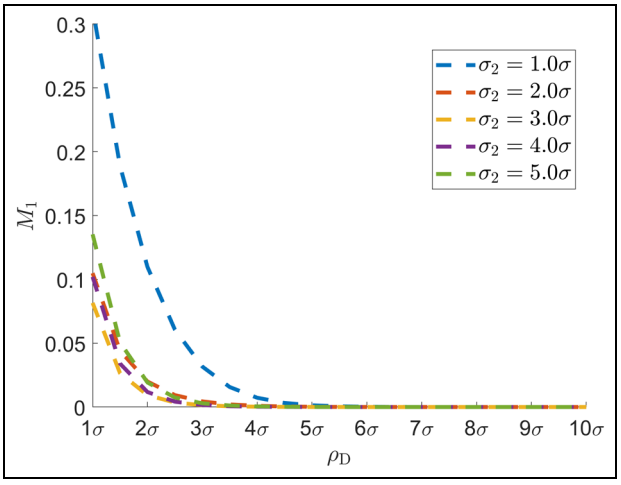

Figure 7. Final mass at $t = 40$ of the attacking drones as a function of the dynamic defense range, ρ_D, for various spreads σ_2. In this scenario, only the dynamic defense is present ($\theta = 0$). Since $\alpha = 0$, $M_2 = 1$ for all time t.

follows from the model formulation where their effectiveness depends only on the total mass and the range of engagement. Within this formulation, tighter formations yield shorter-duration combat (due to the limited spatial reach) with high intensity, whereas wider formations result in longer, lower-intensity combat.

Next, we will focus on the dynamic defense results from Figure 6, which are shown with dashed curves. The mass M_1 varies with the spread of the dynamic defense, with the greatest variation in the short-range case as shown in Figure 6(a) and the least variation in the long-range case as shown in Figure 6(c). Note that the medium-range case ($\rho_D = 3.0\sigma$) in Figure 6(b) with $\sigma_2 = 1.0\sigma$ is identical to the $\rho_D = 3.0\sigma$, case of Figure 5, which uses the reference width of $\sigma_2 = 1.0\sigma$.

For the short-range dynamic defense case of Figure 6(a), a spread of 3σ maximizes attrition at $t = 40$, revealing a trade-off between distribution height, spread (width), and range. While for a spread of 1.0σ, the attrition is minimized as the trailing dynamic defense does not fully engage with the attacking force.

For the long-range dynamic defense case of Figure 6(c), the mass M_1 suffers significant attrition. Spread has minimal effect on the time evolution since spatial dependence matters less at longer ranges. Notably, artifacts of the $\rho_D \to \infty$ limit begin to emerge at this range, namely the exponential solutions in Equation (10).

Figure 7 shows the mass of the attackers once they reach the target at $t = 40$ in the dynamic-only defense case as a function of the range ρ_D and for various spreads, σ_2. The terminal values of the dashed curves in Figure 6(a)–(c) correspond to points on the curves in Figure 7, where $\rho_D = 1.0\sigma$, 3σ, and 10σ. In each case of σ_2, the mass of the attacker decreases monotonically with increased range. We see a minimal effect of ρ_D on M_1 for long range. At short range (e.g., $\rho_D = 1.0\sigma$), the behavior of $\sigma_2 = 1.0\sigma$ is very different from the rest. In this case, the defense is concentrated and has extremely short range. As discussed in section 3.2, this short range limits the defensive capability as it trails the attackers. This suggests an interesting relationship between tracking and range that results in nontrivial outcomes and may warrant future analysis.

3.4. Expendable dynamic defense at infinite range

Next, we consider the situation where the dynamic defense is reduced as it engages with the attacking force, in contrast to the nonexpendable dynamic defense. The expendability parameter α in Equation (6) models this effect. As discussed in section 2, the dynamic defense takes more losses than the attacker takes (from the dynamic defense) when $\alpha > 1$, while $\alpha < 1$ corresponds to the case where losses of the defender are less than losses inflicted on the attacker. When $\alpha = 1$, there is a one-to-one loss, modeling the case where each attacker loss due to the dynamic defense leads to a loss for the dynamic defense.

The simulations in this section will use the same starting locations from section 3.1, defined as the centers of the attacking force (f_1), the dynamic defense (f_2), and the static defense (f_3) distributions. The center positions for these three are $x_1 = 5$, $x_2 = 30$, and $x_3 = 22.5$, respectively. The results presented in this section are not sensitive to these initial conditions since we are now considering effectively infinite interaction ranges, $\rho_D = \rho_S = 10^3\sigma$.

Figure 8 shows the outcome of engagements involving the attacking force versus a dynamic defense ($\theta = 0$) at effectively infinite range (using $\rho_D = 10^3\sigma$). This assumption nullifies the spatial dependence in our model, reducing the governing equations to the area fire model in Equations (3) and (4). Plots of the dynamic defense mass (M_2) versus the attacking force mass (M_1) are called trajectories plotted in phase space. In Figure 8, we observe linear trajectories that illustrate the well-known linear law of the classical Lanchester area fire model. The $\alpha = 1$ case shown in the figure is given by $M_1 = M_2$, corresponding to a one-to-one offense-defense attrition ratio. As expected, values of $\alpha > 1$ lead to steeper slopes, with greater losses to the dynamic defense and fewer losses to the attacking force. When $\alpha < 1$, the dynamic defense eliminates the attacking force with greater efficiency. In the case of $\alpha = 0$ (i.e. the nonexpendable dynamic defense), the defenders take no losses so M_2 does not change.

Figure 9, on the other hand, shows trajectories in phase space for the mixed dynamic-static defense with equally distributed firepower ($\theta = 0.5$). Here, we see the influence of the static defense. Comparing Figure 9 with Figure 8,

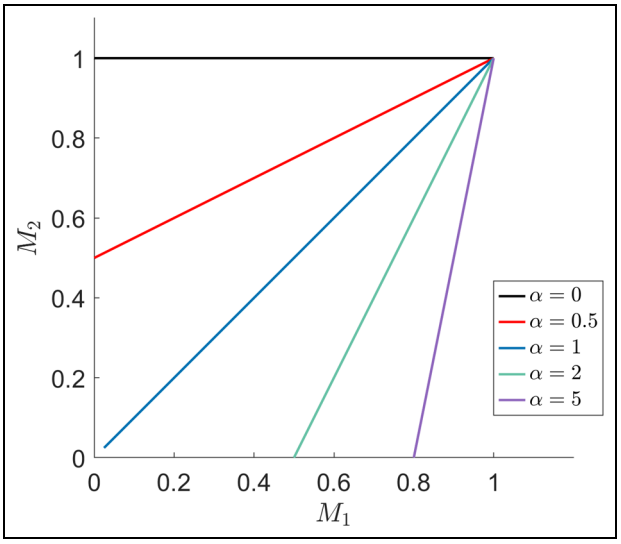

Figure 8. Trajectories of M_2 versus M_1 for different values of α for the dynamic-only defense case ($\theta = 0$) with effectively infinite interaction range, $\rho_D = 10^3\sigma$.

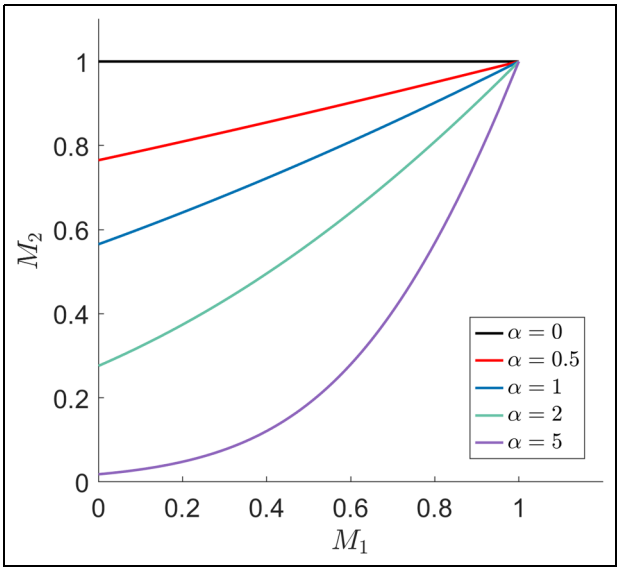

Figure 9. Trajectories of M_2 versus M_1 for different values of the expendability parameter α for the mixed dynamic-static defense ($\theta = 0.5$) with an effectively infinite interaction range $\rho_S = \rho_D = 10^3\sigma$.

the dynamic defense does not suffer the same losses, due to the support provided by the static defense. For example, the $\alpha = 1$ case now leads to a final mass $M_2 \sim 0.57$ in Figure 9, while in Figure 8, the mass M_2 approaches zero. Other than the $\alpha = 0$ case, none of the results shown in Figure 9 are truly linear, although they might appear to be from the figure itself.

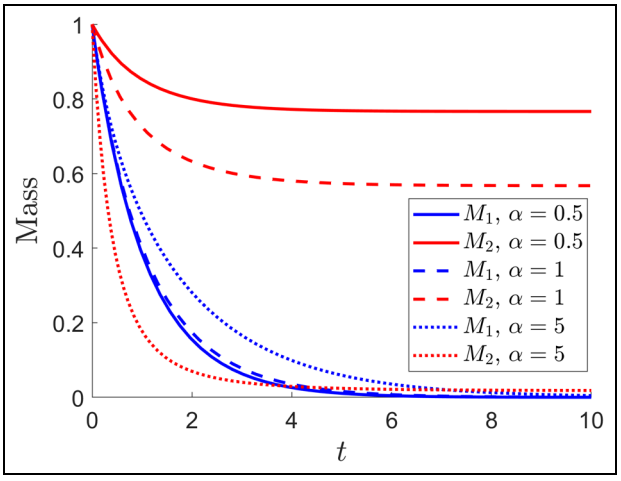

Figure 10. Time evolution plots for total mass of the attacking force (M_1) and the dynamic defense (M_2) for various values of expendability parameter α. The overall defense is mixed dynamic-static ($\theta = 0.5$) with infinite interaction range.

Figure 10 contains time evolution plots of the total masses M_1 and M_2 for three different values of the expendability parameter α. The results shown in Figure 10 have corresponding trajectories in Figure 9. The mass of the dynamic defense, M_2, is more sensitive to changes in α than the mass of the attacking force, M_1. The reason for this is that the losses to M_2 are only due to interactions between the dynamic defense and the attacking force, with losses to M_2 dependent on α. Losses to M_1 are not only due to interactions with the dynamic defense but also due to interactions with the static defense (and the static defense is never reduced in our current model). In other words, the combination of the dynamic and static defenses, acting at effectively infinite ranges, leads to similar overall behavior of M_1 relative to M_2, even with changes to α.

3.5. Expendable dynamic defense at finite range

Section 3.4 discussed expendable dynamic defenders with infinite (or approximately infinite) interaction ranges. In this section, we will consider expendable dynamic defenders with static defenders at finite interaction ranges ($\rho_S = \rho_D = 3\sigma$).

We will now consider different initial conditions in terms of placement of the attackers and defenders in the domain. The attacking force is centered at $x = 5$, moving with a constant velocity of $u_1 = 1$ (to the right). To provide a more complete set of interaction conditions, the initial conditions for the dynamic and static defenses will be adjusted. For example, the dynamic defense will now begin centered at different positions. In addition, although the dynamic defense moves with a velocity determined by

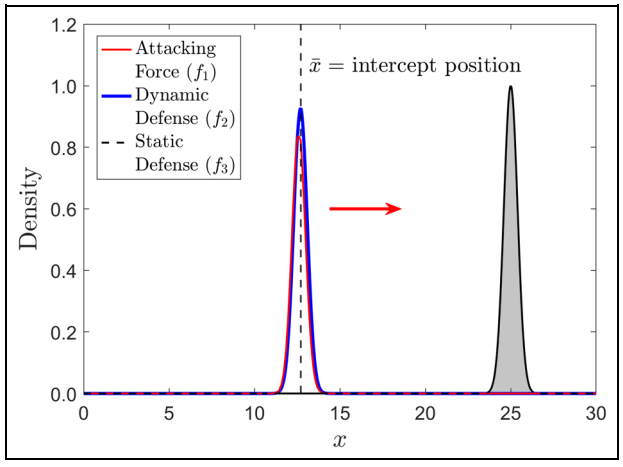

Figure 11. The densities of the attacking force (f_1), dynamic defense (f_2), and static defense (f_3) at the time when the centers of mass of f_1 and f_2 are aligned. This location is called the intercept position, $\bar{x}$.

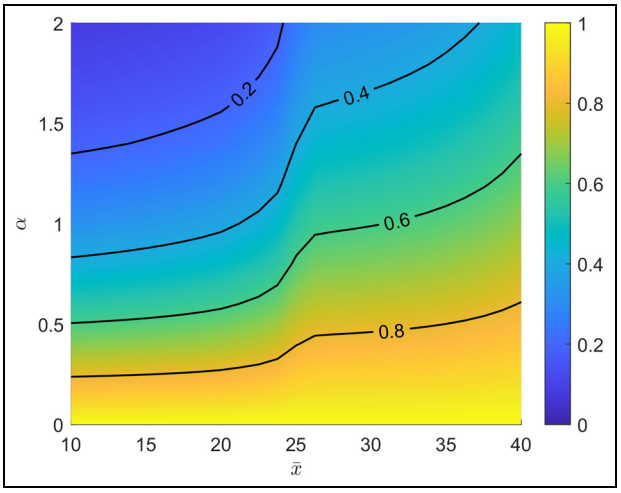

Figure 13. Total mass of the dynamic defense, M_2 after the attackers have reached their target, for various values of α and $\bar{x}$ ($\theta = 0.5$ and $\rho_S = \rho_D = 3\sigma$).

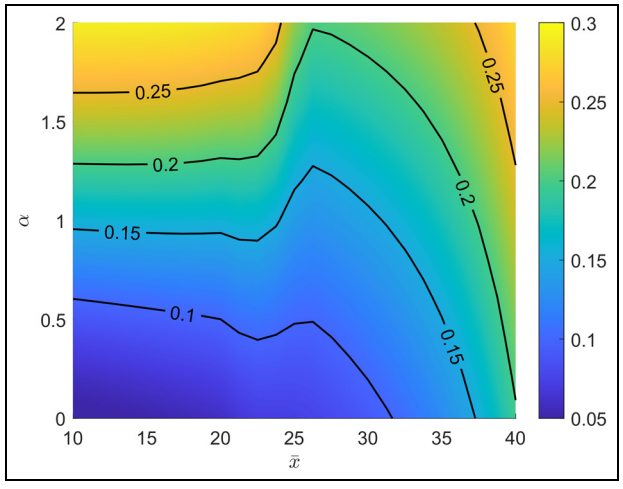

Figure 12. Total mass of the attackers, M_1, after reaching the target for various values of α and $\bar{x}$ ($\theta = 0.5$ and $\rho_S = \rho_D = 3\sigma$).

Equation (7), in some cases, its initial motion will be delayed for a specified time. The different initial positions and time delay (if applied) determine the position where the attacking force and the dynamic defense first interact. Figure 11 shows an instant in time from a single simulation where f_1, moving to the right, is aligned center-to-center with f_2, which had been moving to the left. The intercept position, $\bar{x}$, is defined to be the location in the domain where the centers of mass of f_1 and f_2 first align with each other; although a number of effects determine $\bar{x}$, it is primarily controlled by initial positions and velocities (including any time delay) of the attackers and dynamic defense. According to Equation (7), the velocity $u_2 = 0$ at this instant.

For simulations shown in this section, the position of the static force is fixed at $x = 25$, the domain center. Based on the initial conditions of the dynamic defense, the intercept position may occur before the attacking force reaches the static defense ($5 \leq \bar{x} < 25$), at the instant the attacking force reaches the static defense ($\bar{x} = 25$), or after the center of the attacking forces passes the center of the static defense ($25 < \bar{x} \leq 40$).

Figures 12 and 13 show contours that represent the resulting masses M_1 and M_2, respectively, after reaching the target (at $t = 40$). Note that the contour ranges differ between the two figures and that constant-contour curves with different values are plotted on each figure. The horizontal axes in each figure show the intercept position ($\bar{x}$) and the vertical axes show the expendability parameter of the dynamic defense (α).

We will begin by considering a nonexpendable dynamic defense ($\alpha = 0$). As shown in Figure 12, when $\alpha = 0$, the attacking force is subject to less attrition as $\bar{x}$ increases since there is less time for interaction to occur. Referring back to Figure 3, the time corresponding to region I increases as $\bar{x}$ increases, so there is less time for the dynamic defense to interact with the attackers and M_1 is not reduced as much as it would otherwise. As shown in Figure 13, when $\alpha = 0$, the dynamic defense is not reduced and $M_2 = 1$ for all intercept locations.

Figure 12 shows an interesting relationship between α, $\bar{x}$, and M_1. The mass M_1 monotonically decreases as α decreases for any fixed value of $\bar{x}$ as shown. However, for a fixed value of α, the mass M_1 is affected by two

conditions: (1) the engagement time between the attackers and the dynamic defense (corresponding to $\bar{x}$) and (2) the relative position of the static defense and the attacking force (only if the attacking force has already engaged with the dynamic defense).

The first condition was previously discussed for the $\alpha = 0$ case. That is, the smaller the value of $\bar{x}$, the more time is available for the attacking force and the dynamic defense to interact with each other. When $\alpha > 0$, more interaction time means not only a greater reduction in M_1, but also a greater reduction in M_2. As M_2 decreases, the dynamic defense loses effectiveness since its ability to causes losses to M_1 depends on its own density f_2 through the reaction term $\mathcal{R}_{1_D}$. In other words, smaller values of $\bar{x}$ mean greater losses to M_1, but also greater losses to M_2 (which reduces the ability of the dynamic defense to engage with the attackers). The second condition is based on the fact that the static defense, when it is finally engaged, causes losses to M_1 without suffering any attrition itself. In scenarios where the static defense engages before the dynamic defense ($\bar{x} > 25$), the static defense preconditions the attackers before the attackers fully engage with the dynamic defense. The dynamic defense is thus more effective and the attrition it suffers (due to $\alpha > 0$) has relatively less of an effect on its ability to engage the attackers. Summarizing these two conditions and their effect on M_1, from the perspective of the defenders, there are potential advantages to engaging the attackers early with the dynamic defense, but there are also advantages with delaying engagement until after the attackers have first encountered the static defense.

Figure 13 focuses on the effect that α and $\bar{x}$ have on the dynamic defense. Its mass, M_2, monotonically increases as $\bar{x}$ increases and as α decreases. This result is more straightforward than the behavior of M_1 since decreasing α and the interaction time with the attacking force (by increasing $\bar{x}$) always reduces losses to the dynamic defense. A summary of the main results presented in this entire section is provided in section 4.

4. Conclusion

In this work, we develop a novel system of coupled PDEs to model engagements between attacking drones and a layered defense consisting of defending drones (a dynamic defense) and a static defense. Using this model, the following features of the defense and their influence on attacker attrition have been examined: spatial spread, interaction range, strength allocation between static and dynamic defenses, and expendability of the dynamic defense.

The influence of spread is more apparent with the dynamic defense than with the static defense due to tracking that prolongs the interaction between the attackers and the dynamic defense. In addition, finite interaction ranges lead to distinct engagement phases (of varying durations) in which the static and dynamic defenses engage either separately or simultaneously. Within the assumptions of the model, increasing the range of the dynamic defense has a greater effect on attacker attrition than increasing the range of the static defense; this effect is also due to tracking. Varying the allocation of static and dynamic defense strengths reveals trade-offs in overall effectiveness.

When the dynamic defense is expendable ($\alpha > 0$) and in the infinite-range limit, the model recovers the classical Lanchester linear law in the absence of a static defense. In contrast, a layered static-dynamic defense yields a nonlinear relationship between attrition of the attacker and attrition of the dynamic defense.

For finite-range cases with $\alpha > 0$, the intercept location $\bar{x}$, which is determined by the velocities and initial positions of the attacker and dynamic defense, plays a critical role in determining overall engagement outcomes. For a given value of α, there is a nonmonotonic relationship between the attacker's final mass and $\bar{x}$.

It should be noted that the results presented in this paper are illustrative conclusions of the underlying model, rather than predictive of real-world outcomes. In addition, the parameters used should be thought of as relative magnitudes in order to study qualitative dynamics rather than as exact representatives of combat. Calibration of the parameters based on real combat data remains an important future direction and is beyond the scope of this work.

This study provides a Lanchester-type framework for modeling modern combat dynamics, and although it accounts for only a single spatial dimension, it can be extended to higher dimensions to analyze more complex attack patterns and maneuvering. Such an extension would require additional assumptions about movement directions, interaction kernels, and tracking behavior in higher spatial dimensions. While the governing equations extend naturally, the increase in spatial dimensions adds both modeling and computational complexity, which necessitates strategic numerical techniques (such as splitting methods) to obtain efficient results. Extending the model to higher spatial dimensions would enable the analysis of evasion, terrain effects, and multidirectional attacks, with the potential to incorporate nonconstant velocities and more sophisticated interaction laws.

Acknowledgments

The authors acknowledge Erika Nyberg and Sophia Simpson, cadets at the United States Military Academy, for their contributions to the project. The views expressed in this document are those of the authors and do not reflect the official policy or position of the United States Army,

the Department of War, the United States Military Academy, or the U.S. Government.

ORCID iDs

Charles Randow https://orcid.org/0009-0005-9781-6325
Ryan H Allaire https://orcid.org/0000-0002-9336-3593
Antonio Mastroberardino https://orcid.org/0000-0002-7195-4851

Funding

The authors received no financial support for the research, authorship, and/or publication of this article.

Declaration of conflicting interests

The authors declared no potential conflicts of interest with respect to research, authorship, and/or publication of this article.

References

1. Lanchester FW. *Aircraft in warfare: the dawn of the fourth arm*. London: Constable Limited, 1916.
2. MacKay N. Lanchester combat models. *Math Today* 2006; 42: 170–178.
3. Deitchman SJ. A Lanchester model of guerrilla warfare. *Oper Res* 1962; 10: 818–827.
4. Bonder S. The Lanchester attrition-rate coefficient. *Oper Res* 1967; 15: 221–232.
5. Taylor JG. Solving Lanchester-type equations for "modern warfare" with variable coefficients. *Oper Res* 1974; 22: 756–770.
6. Taylor JG. *Lanchester-type models of warfare. Volume I*. Technical report ADA090842, October 1980. Monterey, CA: Naval Postgraduate School.
7. Taylor JG. *Lanchester-type models of warfare. Volume II*. Technical report ADA090843, October 1980. Monterey, CA: Naval Postgraduate School.
8. Taylor JG. Annihilation prediction for Lanchester-type models of modern warfare. *Oper Res* 1983; 31: 595–606.
9. Taylor JG and Brown GG. Canonical methods in the solution of variable-coefficient Lanchester-type equations of modern warfare. *Oper Res* 1976; 24: 44–69.
10. Taylor JG and Parry SH. Force-ratio considerations for some Lanchester-type models of warfare. *Oper Res* 1975; 23: 522–533.
11. Protopopescu V, Santoro RT, Dockery J, et al. *Combat modeling with partial differential equations*. Technical report ORNL/TM-10636, November 1987. Oak Ridge, TN: Oak Ridge National Laboratory.
12. Protopopescu V, Santoro RT and Azmy YY. PDE models for combat: Potential applications to LIC. In: *Proceedings of the first annual symposium on special operations/low intensity conflict (SO/LIC)*. Alexandria, VA: American Defense Preparedness Association, 1989.
13. Protopopescu V, Santoro R, Cox R, et al. *Combat modeling with partial differential equations: The bidimensional case*. Technical report ORNL/TM-11343, January 1990. Oak Ridge, TN: Oak Ridge National Laboratory.
14. Protopopescu V, Santoro R and Dockery J. Combat modeling with partial differential equations. *Eur J Oper Res* 1989; 38: 178–183.
15. Keane T. Combat modelling with partial differential equations. *Appl Math Model* 2011; 35: 2723–2735.
16. Mogilner A and Edelstein-Keshet L. A non-local model for a swarm. *J Math Biol* 1999; 38: 534–570.
17. Fasana K. *Why drones have revolutionized warfare: drone quasi-maneuver attributes in the offense-defense balance*. Technical report 3000572, April 2024. Alexandria, VA: Institute for Defense Analysis.
18. Spradlin C and Spradlin G. Lanchester's equations in three dimensions. *Comput Math Appl* 2007; 53: 999–1011.
19. Lam MAYH, Cummings LJ and Kondic L. Computing dynamics of thin films via large scale GPU-based simulations. *J Comput Phys X* 2019; 2: 100001.
20. Allaire RH, Cummings LJ and Kondic L. Influence of thermal effects on the breakup of thin films of nanometric thickness. *Phys Rev Fluids* 2022; 7: 064001.

Appendix

A. Analytical results

A1. Modified Lanchester equations. From Equations (8) and (9) in the main text, we obtain an ODE relating the masses of the attacking force and the dynamic defense in the form

$$\frac{dM_1}{dM_2} = \frac{1}{\alpha}\left(1 + \frac{k_3 M_3}{k_2 M_2}\right) \tag{11}$$

where M_3 is the mass of the static defense that remains constant at one. We substitute this value into Equation (11) and solve by separating variables

$$\int_0^t \alpha M_1 d\tau = \int_0^t \left(1 + \frac{k_3}{k_2 M_2}\right) d\tau$$

which has solution

$$\begin{aligned} &\alpha(M_1(t) - M_1(0)) \\ &= M_2(t) - M_2(0) + \tfrac{k_3}{k_2}(\ln M_2(t) - ln\, M_2(0)) \end{aligned} \tag{12}$$

Substituting the initial masses $M_1(0) = M_2(0) = 1$ into Equation (12) and solving for $M_1(t)$ yields the explicit relation

$$M_1(t) = \frac{1}{\alpha}\left(M_2(t) + \frac{k_3}{k_2}\ln M_2(t)\right) + \frac{\alpha - 1}{\alpha}$$

between the masses of the attacker and the dynamic defense in the case of infinite range.

Table 2. Model parameters used in the simulation.

Parameter	Value
Domain length	$L = 50$
Means	$x_1 = 5$, $x_2 = 35$
Diffusion coefficients	$\mathcal{D}_1 = \mathcal{D}_2 = 0.0001$
Reaction rates	$k_2 = k_3 = 0$
Velocities	$u_1 = 1$, $u_2 = -1$, $u_{\max} = 1$

A2. Advection–diffusion equation. Consider the following governing PDE and initial condition for the advection–diffusion problem, which will be used to examine convergence of our code:

$$\frac{\partial f_1}{\partial t} + u_1 \frac{\partial f_1}{\partial x} = \mathcal{D}_1 \frac{\partial^2 f_1}{\partial x^2}$$
$$f_1(x, 0) = \exp\left(-\pi(x - x_1)^2\right)$$

As introduced in Equations (5) and (6), we will solve for f_1 and consider u_1 and $\mathcal{D}_1$ to be constant. The initial condition $f_1(x, 0)$ is the Gaussian profile discussed in section 2 with $\sigma = 1/\sqrt{2\pi}$. We can transform to a moving reference frame using $\xi = x - u_1 t$ to obtain the following diffusion equation and initial condition:

$$\frac{\partial f_1}{\partial t} = \mathcal{D}_1 \frac{\partial^2 f_1}{\partial \xi^2}$$
$$f_1(\xi, 0) = \exp\left(-\pi(\xi - x_1)^2\right)$$

This may be solved using a Fourier transform approach to obtain the solution to our original advection–diffusion problem:

$$f_1(x, t) = \frac{1}{\sqrt{1 + 4\pi\mathcal{D}_1 t}} \exp\left(\frac{-\pi(x - x_1 - u_1 t)^2}{1 + 4\pi\mathcal{D}_1 t}\right)$$

The same form of the solution to f_1 holds for f_2, which would include the terms x_2 and $\mathcal{D}_2$. Table 2 includes the parameters used to compare the analytical (exact) solution to our numerical (computational) results. The relative error, using the L^2 error, is given by

$$\mathcal{E} = \frac{\sqrt{\sum_{i=1}^{N} \left(f_{1,i}^{\text{comp}} - f_{1,i}^{\text{exact}}\right)^2}}{\sqrt{\sum_{i=1}^{N} \left(f_{1,i}^{\text{exact}}\right)^2}}$$

Appendix Figures 14 and 15 show convergence plots for f_1 and f_2, using the relative L^2 error. In Appendix Figure 15, the time step is held constant at $\Delta t = 1 \times 10^{-4}$, while in Appendix Figure 15, the grid spacing is held constant at $\Delta x = 6.25 \times 10^{-4}$. Fixing the time step leads to slopes for the densities of $f_1 \sim 1.49$ and $f_2 \sim 1.55$. Fixing the grid spacing leads to slopes of ~ 1.98 for both densities f_1 and f_2. The sub-quadratic spatial convergence is likely due to the use of a flux-limiter that adaptively switches from the spatially first-order upwind scheme to the second-order scheme in smooth regions. In contrast, the quadratic convergence in time shows that van Leer advection behaves nearly quadratic in time for smooth solutions.

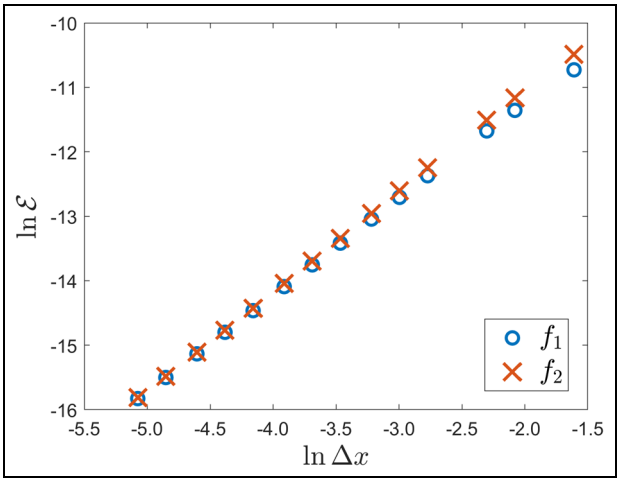

Figure 14. Convergence plot for the advection–diffusion form of the numerical algorithm, holding $\Delta t = 1 \times 10^{-4}$ constant, for f_1 and f_2. Approximate slopes for the two densities are $f_1 \sim 1.49$ and $f_2 \sim 1.55$.

A3. Reaction equation. Consider the reaction equation for f_1:

$$\frac{\partial f_1}{\partial t} = -k_3 f_1 \int_\Omega \frac{1}{2}\left(1 + \cos\left(\frac{\pi(x - y)}{\rho_S}\right)\right) f_3 \, dy$$

and the initial condition

$$f_1(x, 0) = \exp\left(-\pi(x - x_1)^2\right)$$

In the limit $\rho_S \to \infty$, the cosine term goes to 1, so that

$$\frac{\partial f_1}{\partial t} = -k_3 f_1 \int_\Omega f_3 \, dy$$

Since f_3 is constant with $\int_\Omega f_3 \, dy = 1$, it follows that

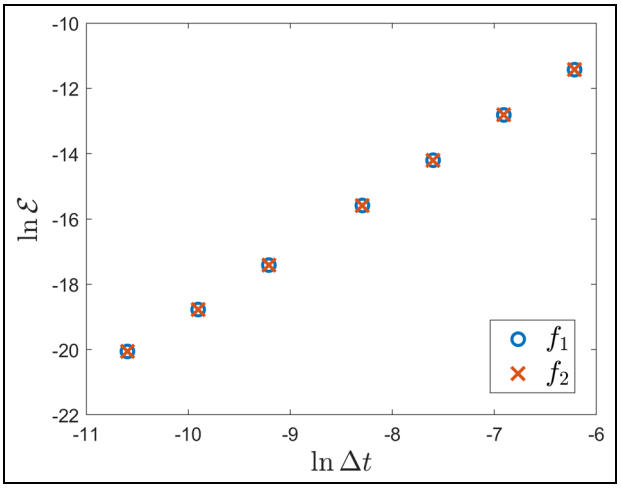

Figure 15. Convergence plot for the advection–diffusion form of the numerical algorithm, holding $\Delta x = 6.25 \times 10^{-4}$ constant, for f_1 and f_2. Approximate slopes for the two densities are both ~ 1.98.

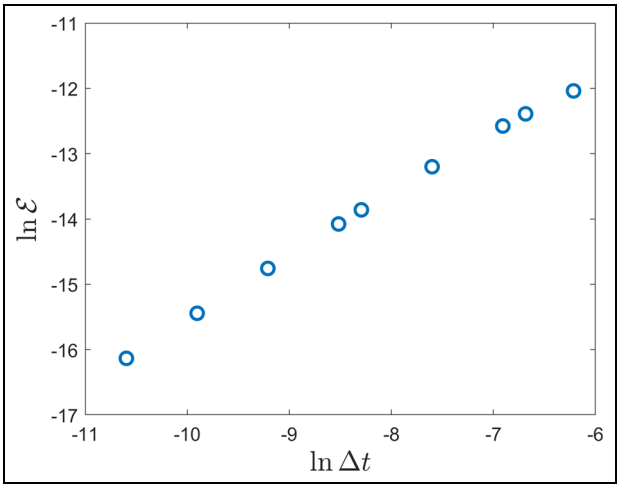

Figure 16. Convergence plot for the reaction-only form of the numerical algorithm, holding $\Delta x = 6.25 \times 10^{-4}$ constant for f_1. The resulting slope is ~ 1.

$$\frac{\partial f_1}{\partial t} = -k_3 f_1$$

The analytical solution to this ODE is as follows:

$$\begin{aligned} f_1(x,t) &= f_1(x,0)\exp(-k_3 t) \\ &= \exp\left(-\pi(x-x_1)^2\right)\exp(-k_3 t) \\ &= \exp\left(-\pi(x-x_1)^2 - k_3 t\right) \end{aligned}$$

Appendix Figure 16 shows the convergence of f_1 using this solution, where $x_1 = 5$ and $k_3 = 1$, and compared with the numerical solution. In the numerical solution, the velocity $u_1 = 0$ and the diffusivity $\mathcal{D}_1 = 0$; to approximate infinite range, the static range is set to $\rho_S = 500 \approx 1250$ with $x_3 = 40$ and a total domain length of 50. The resulting slope for the density f_1 is ~ 1, which is consistent with its Forward Euler time integration.

A4. Advection–reaction, static defense solution. Here, we consider Equation (5), when only the static defenders are present and without diffusion. In this case, Equation (5) becomes

$$\frac{\partial f_1}{\partial t} + u_1 \frac{\partial f_1}{\partial x} = -k_3 f_1 \Phi(x) \tag{13}$$

where $\Phi(x) = (K_S * f_3)(x)$ is the time-independent convolution between the static kernel and f_3. We define the characteristics $x(t) = x_0 + u_1 t$, with initial position x_0 at $t = 0$ as the solution of $dx/dt = u_1$. Then, Equation (13) can be written as

$$\frac{d}{dt} f_1(x(t),t) = -k_3 f_1(x(t),t)\Phi(x(t))$$

which is a separable ODE with the solution

$$f_1(x(t),t) = f_1(x_0,0)\exp\left(-k_3 \int_0^t \Phi(x_0 + u_1 z)\, dz\right)$$

which can be recast into

$$f_1(x,t) = f_1(x - u_1 t, 0)\exp\left(\frac{k_3}{u_1}\int_x^{x-u_1 t} \Phi(\xi) d\xi\right) \tag{14}$$

where $\xi = x_0 + uz$. This says that the solution f_1 is a shift of its initial condition modified in time by an exponential factor related to the static defense. Since f_3 is independent of time, we easily plot M_1 for various values of σ_3 in Appendix Figure 17, closely resembling the solid curves of Figure 6(b). An interesting result is that with Equation (14), we can derive an approximation for the attacker's final mass $M_1(t = 40) \approx \exp(-k_3 \rho_S / u_1)$, since our domain is large. The expression $\exp(-\rho_S)$ gives good agreement with the results in Figure 6.

B. Numerical algorithm

Here, we discuss the numerical algorithm used to solve Equations (5) and (6) of the main text. For clarity, we rewrite the underlying equations here in compact form:

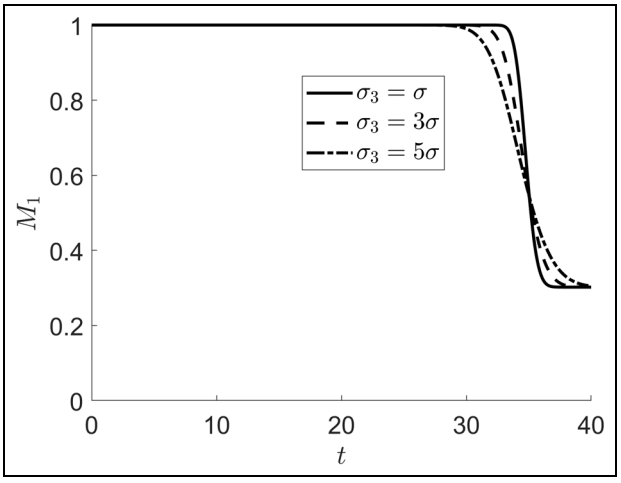

Figure 17. Total mass of the attackers, M_1 based on the analytical solution given in Equation (14) for various values of initial spread.

$$\partial_t \boldsymbol{f} + \partial_x \boldsymbol{J} = \boldsymbol{D}\partial_{xx}\boldsymbol{f} - \boldsymbol{R} \tag{15}$$

where $\boldsymbol{f} = [f_1, f_2]^T$ denotes the vector of unknowns and $\boldsymbol{J} = [u_1 f_1, u_2 f_2]^T = \boldsymbol{U}\boldsymbol{f}$ is the flux vector, with $\boldsymbol{U} = diag(u_1, u_2)\boldsymbol{f}$. The 2×2 diagonal matrix of diffusivities is $\boldsymbol{D} = diag(\mathcal{D}_1, \mathcal{D}_2)$ is, and $\boldsymbol{R} = [\mathcal{R}_1, \mathcal{R}_2]^T$ is a vector of reaction terms. We begin by discretizing the spatial domain Ω into $N_x + 1$ points

$$x_i = i\Delta x, \quad i = 0, 1, 2, \ldots, N_x$$

and define the grid function $\boldsymbol{f}_i^n \approx \boldsymbol{f}(x_i, t_n)$, where $t_n = n\Delta t$, $n = 0, 1, 2, \ldots$. Then, following the work of Lam et al.,[19] for any $\Gamma \subseteq \Omega$, we can express the average value of $\partial_t \boldsymbol{f}$ on Γ as

$$\begin{aligned}\overline{\partial_t \boldsymbol{f}} &= \tfrac{1}{A}\textstyle\int_\Gamma \partial_t \boldsymbol{f}\, dx \\ &= \tfrac{1}{A}\left[\textstyle\int_\Gamma -\partial_x \boldsymbol{J}\, dx + \int_\Gamma \boldsymbol{D}\partial_{xx}\boldsymbol{f}\, dx - \int_\Gamma \boldsymbol{R}\, dx\right]\end{aligned}$$

where A is the length of Γ. In particular, we let $\Gamma = \Omega_i = [x_{i-1/2}, x_{i+1/2}]$ be the interval centered at x_i with length $A = \Delta x$. Then, the average value of $\partial_t \boldsymbol{f}$ on Ω_i is

$$\overline{\partial_t \boldsymbol{f}} = \frac{1}{A}\left[\int_{x_{i-1/2}}^{x_{i+1/2}} -\partial_x \boldsymbol{J}\, dx + \int_{x_{i-1/2}}^{x_{i+1/2}} \boldsymbol{D}\partial_{xx}\boldsymbol{f} - \boldsymbol{R}\, dx\right]$$

The final term can be approximated at the cell-center by using the midpoint rule and the flux term (involving $\boldsymbol{J}$) can be simplified using the fundamental theorem of calculus to yield

$$\overline{\partial_t \boldsymbol{f}} = -\frac{\boldsymbol{J}\left(\boldsymbol{f}_{i+1/2}\right) - \boldsymbol{J}\left(\boldsymbol{f}_{i-1/2}\right)}{\Delta x} + \left(\boldsymbol{D}\partial_{xx}\boldsymbol{f} - \boldsymbol{R}\right)\big|_{x=x_i} \tag{16}$$

Furthermore, the cell-averaged value $\overline{\boldsymbol{f}}$ can be approximated by $\boldsymbol{f}_i$ to second-order accuracy ($\boldsymbol{f}_i = \left(\boldsymbol{f}_{i+1/2} + \boldsymbol{f}_{i-1/2}\right)/2 + \mathcal{O}(\Delta x^2)$). Then, Equation (16) can be written as the dynamical system

$$\frac{d\boldsymbol{f}_i}{dt} = -\frac{1}{\Delta x}(\boldsymbol{J}_+ - \boldsymbol{J}_-) + \boldsymbol{D}\partial_{xx}\boldsymbol{f}|_{x=x_i} - \boldsymbol{R}|_{x=x_i} \tag{17}$$

where $\boldsymbol{J}_+ = \boldsymbol{U}\boldsymbol{f}|_{x=x_{i+1/2}}$ and $\boldsymbol{J}_- = \boldsymbol{U}\boldsymbol{f}|_{x=x_{i-1/2}}$. Note that various approximations to $\boldsymbol{J}_+$ and $\boldsymbol{J}_-$ exist. For example, choosing $\boldsymbol{J}_+ = \boldsymbol{U}_{i+1/2}\boldsymbol{f}_i$ yields the first-order upwind scheme, which is stable but leads to large amounts of numerical diffusion. Choosing $\boldsymbol{J}_+ = \boldsymbol{U}_{i+1/2}\left(\boldsymbol{f}_i + \boldsymbol{f}_{i+1}\right)/2$ ensures second-order accuracy of the advective term at the cost of oscillations near steep gradients. Instead, we use a van Leer flux limiter, which balances these two. At each interface, $x_{i+1/2}$, we write (in component form)

$$(J_k)_{i+1/2} = (u_k)_{i+1/2}\begin{cases} (f_k)_i + \frac{1}{2}(s_k)_i & \text{if } (u_k)_{i+1/2} > 0 \\ (f_k)_{i+1} - \frac{1}{2}(s_k)_{i+1} & \text{if } (u_k)_{i+1/2} < 0 \end{cases} \tag{18}$$

for $k = 1, 2$ (corresponding to f_1 and f_2, respectively) and $i = 1, \ldots, N_x - 1$, where $(s_k)_i$ is the slope in cell i computed with the limiter

$$(s_k)_i = \phi_k(r_i)\frac{(f_k)_{i+1} - (f_k)_{i-1}}{2}$$

where $\phi(r) = (r + |r|)/(1 + |r|)$ is a scaling of the slope s_i and for a given force k, $r_i = (f_{i+1} - f_i)/(f_i - f_{i-1})$ measures how smooth the solution is at point x_i. Similar equations apply at interface $x_{i-1/2}$. The velocity is approximated to second order as $(u_k)_{i+1/2} = \left((u_k)_i + (u_k)_{i+1}\right)/2$. The first case in Equation (18) corresponds to a wave moving to the right, whereas the second is the case of a wave moving to the left.

The main idea is that $\phi \sim 1$, when $r \sim 1$ (the function is smooth there and we can use the second-order scheme $s_i \sim (f_{i+1} - f_{i-1})/2$. When $r \leq 0$, we have $\phi = s_i = 0$ and the advection scheme is then first-order upwind, attempting to handle sharp fronts.

At the lateral boundaries, $x = 0, L$, we implement outflow (and no-inflow) conditions:

$$(J_k)_{1/2} = \begin{cases} 0, & (u_k)_1 \geqslant 0 \\ (u_k)_1 (f_k)_1, & (u_k)_1 < 0 \end{cases}$$
$$(J_k)_{N_x+1/2} = \begin{cases} 0, & (u_k)_{N_x} \leq 0 \\ (u_k)_{N_x} (f_k)_{N_x}, & (u_k)_{N_x} > 0 \end{cases}$$

where the first conditions are for inflow and the second are for outflow, effectively setting a zero exterior flux for inflow and standard upwinding for outflow. The convolutions in the reaction term $\boldsymbol{R}$ are approximated using the midpoint rule (effectively turning the continuous convolutions into discrete ones).

Although Equation (17) can be time-integrated in various ways, we use an implicit–explicit scheme. We use Crank–Nicolson (CN) for diffusion and Forward Euler on the remaining terms (advection and reaction). Higher-order Runge–Kutta methods could also be implemented on the explicit terms. For example, Allaire et al.[20] utilize a Runge–Kutta, order 2, implicit–explicit scheme on diffusion-like equations to preserve second-order accuracy, but circumvent the added computational complexity of a predictor-corrector with parallelization. In our case, the flux limiter may reduce the order of error to $\mathcal{O}(\Delta t)$ in time anyway, so higher-order limiters would also be needed to preserve second-order accuracy. For our purposes, a lower-order Forward Euler is found to be acceptable with sufficiently high resolution. The chosen time-discretization leads to the following linear system to solve

$$\boldsymbol{A}\boldsymbol{f}^{n+1} = \boldsymbol{B}\boldsymbol{f}^n + \Delta t(\mathcal{A}^n - \boldsymbol{R}^n) \tag{19}$$

where $\boldsymbol{A} = \text{blkdiag}(\boldsymbol{I} - \mathcal{D}_1 \boldsymbol{L}\Delta t/2, \boldsymbol{I} - \mathcal{D}_2 \boldsymbol{L}\Delta t/2)$, $\boldsymbol{B} = \text{blkdiag}(\boldsymbol{I} + \mathcal{D}_1 \boldsymbol{L}\Delta t/2, \boldsymbol{I} + \mathcal{D}_2 \boldsymbol{L}\Delta t/2)$ are block diagonal matrices and $\mathcal{A} = -(\boldsymbol{J}_+ - \boldsymbol{J}_-)/\Delta x$ for discrete Laplacian matrix $\boldsymbol{L}$ (corresponding to Neumann boundary conditions) and identity matrix $\boldsymbol{I}$. Equation (19) is solved using the built-in *mldivide* solver in MATLAB.

Author biographies

Charles Randow is an Assistant Professor of Mathematical Sciences at the United States Military Academy (West Point). Before coming to West Point, he worked at the Army Research Laboratory after earning his PhD in engineering science and mechanics from the Pennsylvania State University.

Ryan H Allaire is an Assistant Professor of Mathematical Sciences at the United States Military Academy. He received his PhD in applied mathematics from the New Jersey Institute of Technology in 2021, where his research focused on the mathematical modeling of thin films using high-performance computing and asymptotic analysis.

Antonio Mastroberardino is an Assistant Professor of Mathematical Sciences at the United States Military Academy. He received his PhD in mathematics from the University at Buffalo after earning degrees in mechanical and aerospace engineering from Cornell University and mathematics from the State University of New York at Brockport. His recent research focuses on mathematical biology, including tumor modeling and tear film dynamics.

Ruixi Luo is a cadet at the United States Military Academy and will graduate in spring 2027. She is majoring in mechanical engineering with a minor in history. She plans to pursue graduate study and continue her research on two-stage rocket flight dynamics.